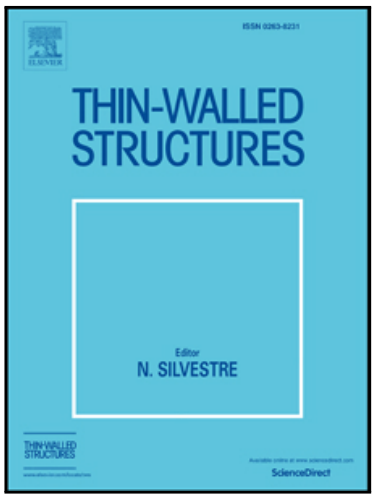

Behaviour and design of bolted aluminium flange cleats

M. CABRERA , M. THEOFANOUS , M. BOCK

PII: S0263-8231(25)00540-3
DOI: https://doi.org/10.1016/j.tws.2025.113447
Reference: TWST 113447

To appear in: *Thin-Walled Structures*

Received date: 17 February 2025
Revised date: 9 May 2025
Accepted date: 12 May 2025

Please cite this article as: M. CABRERA , M. THEOFANOUS , M. BOCK , Behaviour and design of bolted aluminium flange cleats, *Thin-Walled Structures* (2025), doi: https://doi.org/10.1016/j.tws.2025.113447

Highlights

- 5 tests on bolted aluminium angle cleats with various failure modes are reported.
- A numerical model including fracture using uniaxial tensile tests on flat and grooved coupons is presented.
- Following validation against test, 20 FE analysis are performed exhibiting various failure modes.
- Results show that the current design model given in EN 1999-1-1 is unsafe.
- A predictive model derived from first principles is proposed that shows reliable predictions.

BEHAVIOUR AND DESIGN OF BOLTED ALUMINIUM FLANGE CLEATS

M. CABRERA [a], M. THEOFANOUS [a] and M. BOCK [b*]

[a] School of Engineering, Department of Civil Engineering, University of Birmingham, Birmingham, UK

Emails: m.cabreraduran@bham.ac.uk, m.theofanous@bham.ac.uk

[b] College of Engineering and Physical Sciences, Department of Civil Engineering, Aston University, Birmingham, UK

Email: m.bock@aston.ac.uk

*Corresponding author

Keywords: aluminium, flange cleats, connections, EN 1999, equivalent T-stub.

Abstract. Equivalent T-stubs are traditionally employed to model the structural behaviour of the tension zone of moment resisting connections. The design model for the equivalent T-stub considers only the bending moments acting on the equivalent T-stub without considering the co-existing tensile force acting on the T-stub web. However, for flange cleats in bending, the horizontal cleat leg (i.e. the T-stub web) at the junction with the vertical leg is subjected to a co-existing tensile force in addition to the bending moment which limits its moment resistance. This is not considered in current design specifications which made them potentially unsafe. This paper reports 5 experimental tests on bolted aluminium angle cleats in grade 6082 T6 that were used to develop and validate a finite element model. Subsequently, parametric studies were conducted over a wider range of flange cleat geometries covering all types of failure modes considered in EN 1999-1-1. The design specifications for equivalent T-stubs in tension set out in EN 1999-1-1 were assessed and cases where the specifications are inaccurate or potentially unsafe were highlighted. A simple modification of the existing design model is proposed, which offers more consistent and safe ultimate capacity predictions.

1. INTRODUCTION

Structural aluminium is becoming increasingly popular in the construction industry owing to its durability, favourable strength to weight ratio, and ease of manufacturability and aesthetics. Structural applications of aluminium alloys have been extended during the past decades and nowadays it is possible to find aluminium used as main load bearing elements in several bridges and buildings [1, 2]. A key element that controls the stiffness, strength, robustness, and often drives overall cost in structures are connections.

The current European design code for application to structural aluminium is EN 1999-1-1 [3], which also provides the rules for connection design in its Annex N. According to this Annex N of EN 1999-1-1 [3], aluminium connections can be designed using the component method outlined in EN 1993-1-8 [4], the part of the structural steel code that deals with steel joint design. The application of the component method allows determining the strength and stiffness of a joint utilising the mechanical features of the single fundamental structural components. Among the typical components of a joint, flange cleats in bending, shown in Figure 1 (a), are listed by the component method as a type of connection to model beam-to-column connections. According to Annex A of EN 1993-1-8 [4], the design resistance of a bolted flange cleat in bending and its associated failure mode, along with their bolts in tension, should be taken as those of an equivalent T-stub of modified dimensions (see Figure 1 (b)) using, however, the formulae given in Annex B of EN 1999-1-1 [3]. In Figure 1 (b) b_{cf} is the overall width of the angle cleat and l_{eff} is the effective length of the equivalent T-stub determined as l_{eff}=0.5b_{cf}.

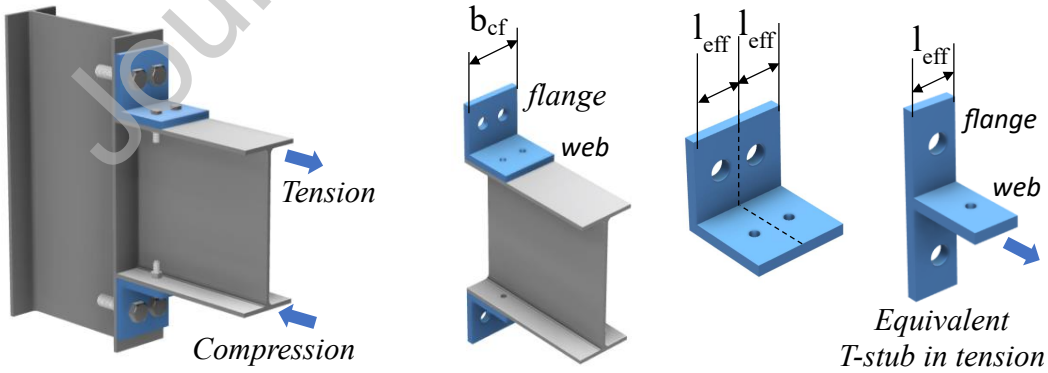

(a) (b)

Figure 1: (a) beam-to-column connection with bolted angle cleats in bending; (b) equivalent T-stub model.

The design model for the T-stub resistance specified in Annex B of [3] is based on the upper bound theorem of plastic analysis. Four possible collapse mechanisms are considered, as shown in Figure 2, and their corresponding collapse loads are determined according to Equations (1)-(4). The minimum of the four collapse loads is the resistance of the angle cleat. Mode 1 refers to plastic failure of the flange, where 4 hinges develop, two at the bolt locations and two at the web to flange junction. Mode 2a refers to plastic failure of the flange at the web to flange junction and simultaneous yielding of the bolts. Mode 2b refers to bolt fracture and yielding of the flange and finally, Mode 3 refers to bolt fracture. The ultimate design resistance for all these possible failure modes can be predicted using Equations (1)-(4), where $M_{u,1}$, $M_{u,2}$ and $M_{o,2}$ are given in Equations (5)-(7), respectively,$1/k$ is a parameter related to the material, B_o and B_u are bolt related strengths given in Equations (8) and (9), where $F_{t,Rd}$ is the design tension resistance and $B_{p,Rd}$ is the design punching shear resistance of the bolt-plate assembly, f_o is the cleat material yield stress, f_u is the material ultimate strength, t_f, g and e_e are variables pertinent to the bolt arrangement of the equivalent T-stub shown in Figure 3 (a), where $e_e \leq 1.25g$. In the absence of welds and hence heat affected zones in the extruded angle cleats considered herein, the $\rho_{u,haz}$ and $\rho_{o,haz}$ coefficients in Equations (5)-(7) equal to one, whilst all partial safety factors γ_M are set to unity to facilitate the comparison between the design predictions and the obtained experimental and numerical resistances. The variables $l_{eff,1}$ and $l_{eff,2}$ for Modes 1 and 2, respectively, are the minimum between the effective length for circular patterns and non-circular patterns of the yield lines that could form.

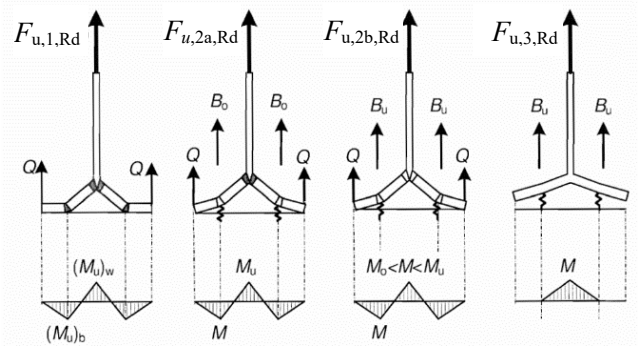

Mode 1 Mode 2a Mode 2b Mode 3

Figure 2: Failure modes of equivalent T- Stub [3].

$$F_{u,1,Rd} = \frac{2\left(M_{u,1}\right)_w + 2\left(M_{u,1}\right)_b}{g} \quad (1)$$

$$F_{u,2a,Rd} = \frac{2M_{u,2} + e_e \sum B_0}{g + e_e} \quad (2)$$

$$F_{u,2b,Rd} = \frac{2M_{o,2} + e_e \sum B_u}{g + e_e} \quad (3)$$

$$F_{u,3,Rd} = \sum B_u \quad (4)$$

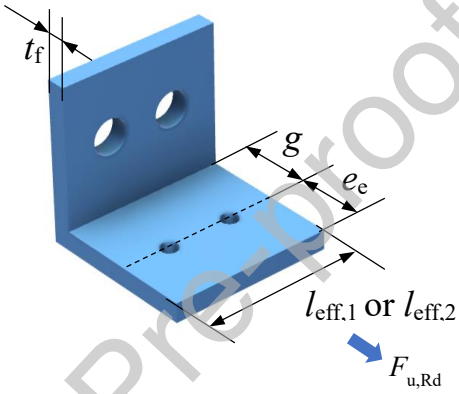

Figure 3: Definition of variables in design formulae.

$$M_{u,1} = 0.25 t_f^2 \sum (l_{eff,1} \rho_{u,haz} f_u) \frac{1}{k} \frac{1}{\gamma_{M2}} \quad (5)$$

$$M_{u,2} = 0.25 t_f^2 \sum (l_{eff,2} \rho_{u,haz} f_u) \frac{1}{k} \frac{1}{\gamma_{M2}} \quad (6)$$

$$M_{o,2} = 0.25 t_f^2 \sum (l_{eff,2} \rho_{o,haz} f_o) \frac{1}{\gamma_{M1}} \quad (7)$$

$$B_o = min \begin{Bmatrix} B_{p,Rd} \\ \frac{0.9 f_y A_s}{\gamma_{M1}} \text{ for steel bolts} \\ \frac{0.9 f_o A_s}{\gamma_{M1}} \text{ for aluminum bolts} \end{Bmatrix} \quad (8)$$

$$B_u = min \begin{Bmatrix} F_{t,Rd} \\ B_{p,Rd} \end{Bmatrix} \quad (9)$$

The structural behaviour of bolted T-stubs has been extensively investigated for several structural metals including carbon steel, high strength steel, and stainless steel whilst research on aluminium T-stubs is yet relatively scarce. Coehlo et al. [5] experimentally investigated the performance of T-stubs made of carbon steel welded plates and assessed relevant design methods for a wide range of T-stub configurations and geometries. Zhao et al. [6] tested a series of T-stubs made of different steel grades including high-strength steel and observed that high strength steel T-stubs offer greater strength but less ductility. A series of experimental and numerical investigations were carried out under both monotonic [7-11] and cyclic loading on stainless steel T-stubs [12] and full-scale connections [13-15] to address the issue of very limited structural data on stainless steel connections. De Matteis et al. conducted a series of tests under monotonic and cyclic loading on aluminium alloy bolted T-stubs [16,17] and carried out parametric studies [18,19]. Xu et al. [20] investigated failure modes on bolted aluminium alloy T-stubs and Wang et al. [21] experimentally examined extruded aluminium alloy T-stubs connected by swage-locking pins.

This paper investigates for the first time the structural response of bolted aluminium alloy angle cleats in tension, which is a common joint arrangement used for semi-rigid joints. Given the adverse effect of welding on aluminium strength and ductility within the heat affected zone [22, 23], utilising a fully bolted configuration for beam-to-column joints is an attractive structural solution. The latest version of EN 1999-1-1 [3] allows the use of the component method specified in EN 1993-1-8 [4] for the design of connections and identifies flange cleats in bending as a typical joint component as above explained, however it does not explicitly cover the design of bolted flange cleats according to its equivalent T-stub model. In addition to this, past studies on bolted carbon steel angle cleats have highlighted that the failure modes of an equivalent T-stub are not representative of the actual failure modes that develop in bolted angle cleats [24, 25], where failure occurs in the web of the angle cleat rather than the flange. This is because the web of the angle cleat carries a tension force that is not considered in the current formulae given by Equations (1) - (9) and presented above.

Allowing for the coexisting axial force when designing aluminium cleats is critical because the design model for aluminium T-stubs allows for a full exploitation of the material strength (ultimate

tensile stress) and hence there is no reserve strength that can be relied upon to accommodate the additional small but non-negligible stresses due to the axial force. Conversely, in steel and stainless steel T-stubs, the design model of EN 1993-1-8 [4] assumes failure to occur when the plastic resistance of the T-stub is reached. Hence it does not allow stresses higher than the yield strength to develop and failure is assumed to occur either when 4 plastic hinges form in the T-stub or earlier if bolt fracture precedes the formation of the 4 plastic hinges. Therefore, sufficient reserve strength is available to accommodate additional tensile stresses.

To address both the lack of structural performance data on bolted aluminium angle cleats and the deficiency of the current method given in EN 1999-1-1 [3], experimental tests followed by a finite element numerical study is utilised in the present investigation to assess the suitability of the T-stub model specified in EN 1999-1-1 [3] to simulate the effect of bolted flange cleats in bending. Based on experimental and numerical data, a new design method is proposed to accurately capture the ultimate design resistance of bolted aluminium angle cleats.

2. EXPERIMENTAL STUDY

A series of experimental tests on bolted aluminium angle cleats in tension was conducted at the Structures Laboratory at the University of Birmingham to obtain fundamental structural performance data and enable the development and validation of numerical models. Since failure of these connections is governed by fracture, material tests, in addition to the standard dog-bone coupons, include flat-grooved specimens to calibrate the fracture model used in subsequent numerical studies.

2.1 Material coupon tests

All material was in grade 6082 T6 which is an alloy included in EN 1999-1-1 [3]. Standard dog-bone coupons were extracted from the same plate used to manufacture the angle cleats with the geometry shown in Figure 4, where a specimen during and after testing is also depicted. Uniaxial tension testing was performed in a 600 kN Avery tension/compression self-reacting frame on two specimens under displacement control with an applied rate of 0.02 mm/s until fracture. Strains were measured over a 50 mm gauge length using an epsilon extensometer.

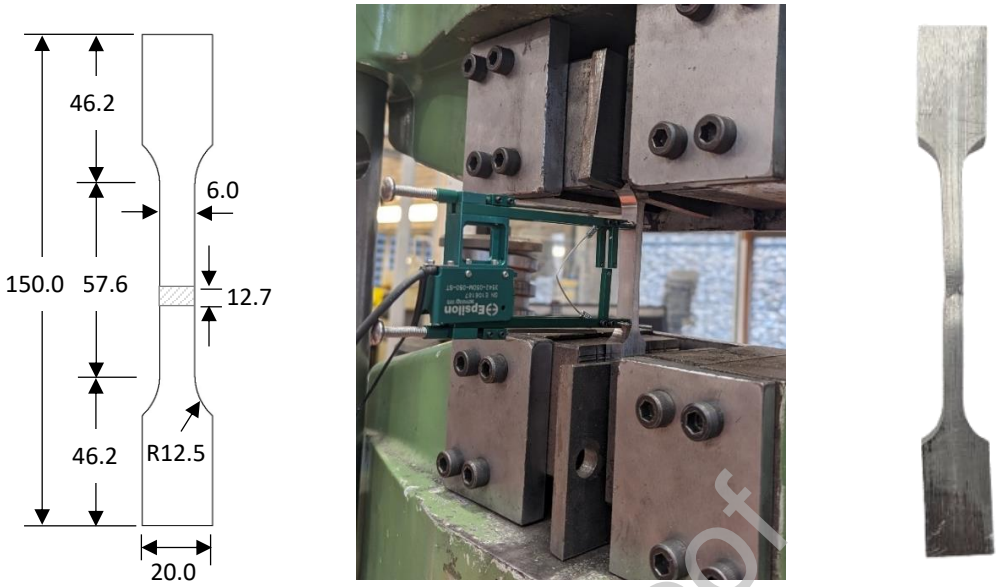

(a) (b) (c)

Figure 4: Dog bone (a) sketch in mm; (b) specimen during testing; (c) after testing.

Figure 5 shows the experimental curve together with an analytical approximation based on the Ramberg-Osgood model. Average material properties obtained from the dog-bone coupon tests are reported in Table 2, where E is the Young's modulus, f_o is the 0.2% proof strength, n is the Ramberg-Osgood exponent that provides a best fit to the experimental curve, f_u is the ultimate stress, ε_u is the strain at ultimate stress, and ε_f the strain at fracture. The nominal f_o, f_u and n given in EN 1999-1-1 for the 6082 T6 alloy are 250 MPa, 290 MPa and 32, respectively, which appear to be conservative based on the experimental results obtained herein and in past experimental studies [26]. Average bolt material properties obtained from tested coupons from the same batch of bolts [27] are also summarized in Table 1.

Table 1. Average material properties of plate and bolt material.

Specimen	E (MPa)	f_o (MPa)	f_u (MPa)	ε_u (%)	ε_f (%)	n
6082 T6	72956	308.0	331.2	6.5	11.1	48
8.8 Bolt	193000	957.0	974.0	4.7	10.1	-

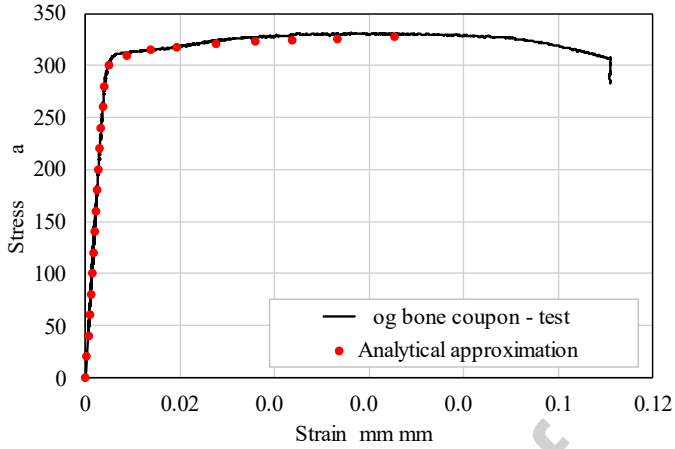

Figure 5: Experimental stress strain response for dog-bone coupons and Ramberg-Osgood approximation.

2.2 Tests on flat grooved coupons

To model material fracture, material tests on coupons subjected to various levels of stress triaxialities need to be conducted [28, 29]. Since all bolted cleat specimens are expected to fail due to tension with minimal effect of shear, no shear material specimens were tested and the developed fracture model incorporated only stress triaxiality dependence. Three flat grooved specimens incorporating a circumferential notch as shown in Figure 6 were conducted. The nominal minimum thickness of specimens at the groove t_0 was set to 5 mm, and the radius of the groove R was varied between 4 and 40mm to obtain a range of levels of stress triaxiality η based on Eq. (10) [27]. All flat grooved specimens have a Lode angle of approximately 0, which is in accordance with the Lode angle of the legs of the flange cleats during testing. The equivalent strain to fracture ε_f in the necking cross section of a flat notched plate can be estimated using the logarithmic measure of the true strain by Eq. (11) [26], where t_f is the measured thickness of the material coupon after fracture. The flat-grooved specimens were labelled with the sized radius R in mm namely R40, R8 and R4.

$$\eta = \frac{\sigma_m}{\bar{\sigma}} = \frac{\sqrt{3}}{3}\left[1 + 2ln\left(1 + \frac{t_0}{4R}\right)\right] \tag{10}$$

$$\varepsilon_f = \frac{2}{\sqrt{3}} ln\left(\frac{t_0}{t_f}\right) \tag{11}$$

(a) (b) (c)

Figure 6: Flat-grooved (a) sketch; (b) specimens with varying R and t_0 before testing; (c) after testing.

Table 2 reports key parameters defined by Equations (10) and (11), while Figure 7 shows the recorded load-extension curves for all coupons. As expected, with increasing stress triaxiality the average maximum stress at the notch increases and the displacement at fracture decreases. The curves shown in Figure 7 are used to calibrate the fracture model as discussed in Section 3.2

Table 2. Geometric configuration, associated stress triaxiality, and key test data for coupons.

Specimen	Stress triaxiality η	Initial thickness t_0 (mm)	Fracture thickness t_f (mm)	Plastic strain at fracture ε_f	Avg. ultimate tensile stress fu (MPa)
Dog bone coupon	0.33	6.01	4.87	-	331
Flat grooved R40	0.61	4.93	3.19	0.50	353
Flat grooved R8	0.75	4.97	3.70	0.34	372
Flat grooved R4	0.89	4.99	4.05	0.22	390

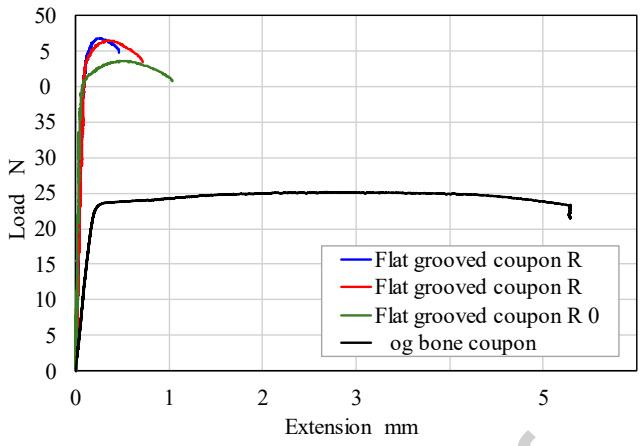

Figure 7: Load-extension curves for 6082 T6 material coupons.

2.3 Tests on bolted flange cleats

Five experimental tests were performed on aluminium angle cleats in Grade 6082 T6 that were manufactured by extrusion and supplied with the dimensions and hole arrangement shown in Figure 8 (a). Two test setups were considered: (i) a single symmetric setup as shown in Figure 8 (b), where the webs of two angle cleats are bolted back-to-back and the flanges are bolted to a rigid plate (R), and (ii) a doubly symmetric setup as shown in Figure 8 (c), where four angle cleats are all bolted back-to-back (S). In both test setups the webs of the angle cleats were bolted to a plate clamped to the grips of the machine that applied tension force which is a setup similar to that applied to the T-stub in tension tested in [5-12] and simulates the tension flange of a beam. In the single symmetric setup (S) the flanges were bolted to a fixed base and is a representative setup for connections between components of similar stiffness; this setup does not lead to the development of membrane action. Setup (R) is representative of a bolted flange connection to a very stiff component (e.g. thick flange of a column), and may lead to significant membrane action and hence enhanced strength if failure occurs at large enough displacements. The measured dimensions of the tested specimens are reported in Table 3 and illustrated in Figure 8 (a). Two bolt types were considered: M10 in Grade 8.8 and M16 in Grade 10.9, in 11mm and 18mm clearance holes, respectively. It is noted that the M16 bolt in Grade 10.9 remained elastic throughout the test. Note that all angle cleats were of constant thickness hence t_w=t_f, and the average values based on three measurements across the web and flange are reported in Table 3.

Table 3. Tested specimen description.

Specimen	Test arrangement	D	d_0 (mm)	b_{cf} (mm)	t_w (mm)	g (mm)	e_e (mm)
M10-6.2-21.6-R-1	Rigid plate	M10	11.0	150	6.19	80.0	21.6
M10-6.2-21.6-R-2	Rigid plate	M10	11.0	150	6.14	80.0	21.6
M10-6.2-41.6-S	Symmetric	M10	11.0	150	6.22	60.0	41.6
M10-12.7-21.6-S	Symmetric	M10	11.0	150	12.6	80.0	21.6
M16-12.7-41.6-S	Symmetric	M16	18.0	150	12.6	60.0	41.6

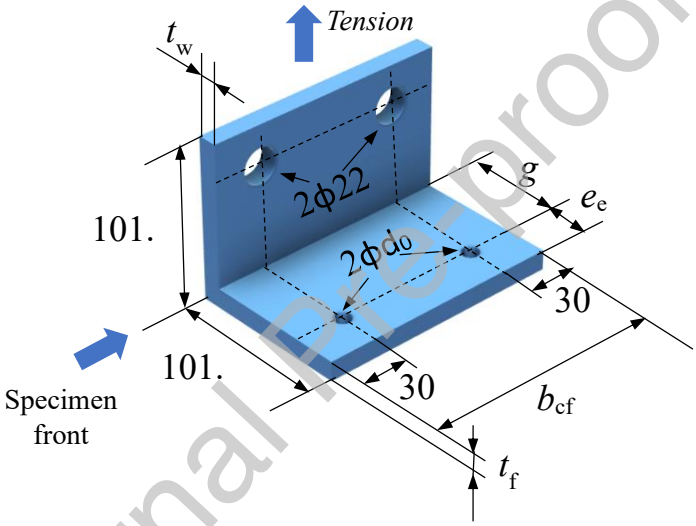

(a)

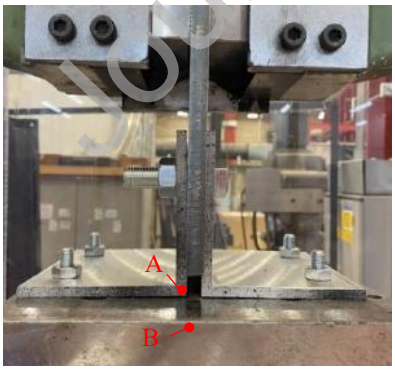

(b)

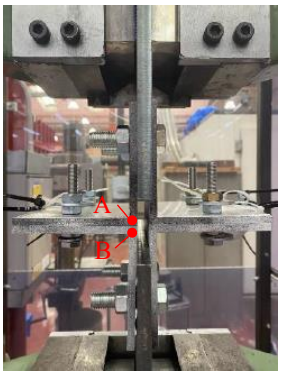

(c)

Figure 8: (a) Angle cleat dimensions in mm; (b) rigid plate arrangement (R); (c) symmetric test arrangement (S).

The instrumentation consisted of the load cell embedded in the Avery machine and a Digital Image Correlation (DIC) system recording full field measurements of displacements and strains in the critical parts of the specimens, except for sample M16-12.7-41.6-S, where LVDTs were installed instead due to a fault in the DIC equipment. Prior to testing, the front part of the specimens was painted white using an elastic paint that can stretch without cracking and a black speckle pattern was sprayed to create the necessary measurement points as shown in Figures 8 (b) and (c). Table 4 reports the failure loads and failure modes for each sample alongside the relevant predictions based on the equivalent T-stub model specified in EN 1999-1-1 [3] using partial safety factor γ_{M1}=1. Wherever cleat fracture occurred, this was always in the web at the flange to web junction due to the superposition of the bending stresses with the tensile stresses transferred by the loading plate. Due to inevitable asymmetries in the setup, fracture always started at the end of one of the flange cleat webs and propagated both longitudinally and through the thickness of the vertical leg of the cleat.

Table . Equivalent T-Stub tensile tests results

Specimen	$F_{u,test}$ (kN)	Failure mode Test	$F_{u,EC9}$ (kN)	Failure mode EC9	$F_{u,EC9}/F_{u,test}$
M10-6.2-21.6-R-1	33.06	Web fracture (W)	24.7	1	0.75
M10-6.2-21.6-R-2	31.12	Web fracture (W)	24.3	1	0.78
M10-6.2-41.6-S	41.15	Web fracture (W)	35.1	1	0.85
M10-12.7-21.6-S	89.69	Bolt fracture (B)	92.8	2b	1.03
M16-12.7-41.6-S	172.3	Web fracture (W)	163.5	1	0.95

Figure 9 shows the recorded load-displacement response for the 5 tested specimens, while the failure modes are depicted in Figure 10. It should be noted that the displacement reported in Figure 9 corresponds to the gap opening (A-B) between the two pairs of the angle cleats for the (S) arrangement or the pair of angle cleat and the reaction rigid T-stub for the (R) as obtained by DIC monitored points A and B in Figure 8 (b) and (c). As expected, the strength of the bolted cleats increased with increasing thickness and e_e distance, as well as with increasing the bolt strength. Furthermore, the EN 1999-1-1 [3] predictions seem overly conservative for the thin specimens and

become less conservative or even unsafe with increasing thickness. This is further investigated numerically in the following section.

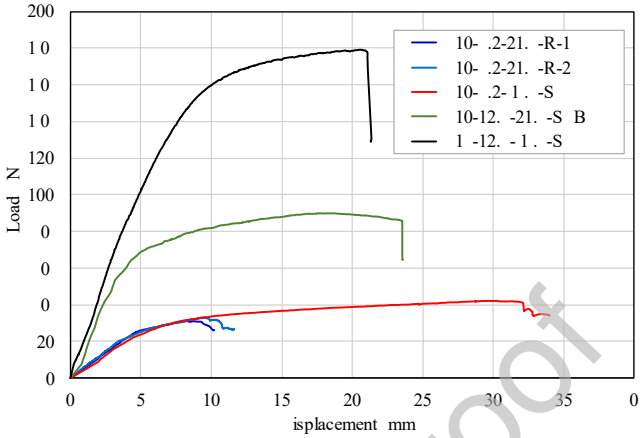

Figure 9: Load-displacement response of tested specimens and failure mode, where W: Web fracture and B: bolt fracture.

Web fracture (W)
(a)

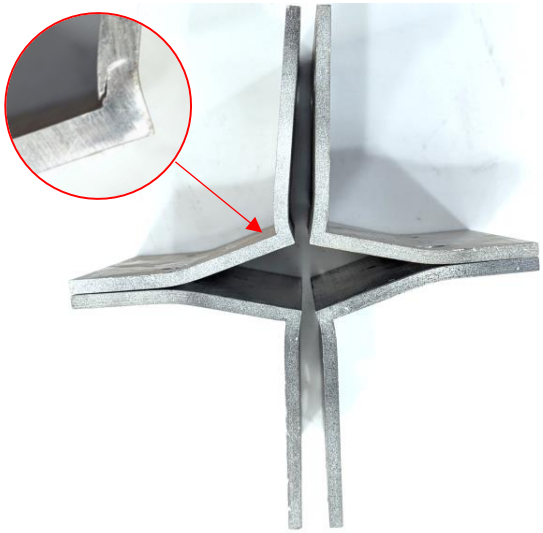

Web fracture (W)
(b)

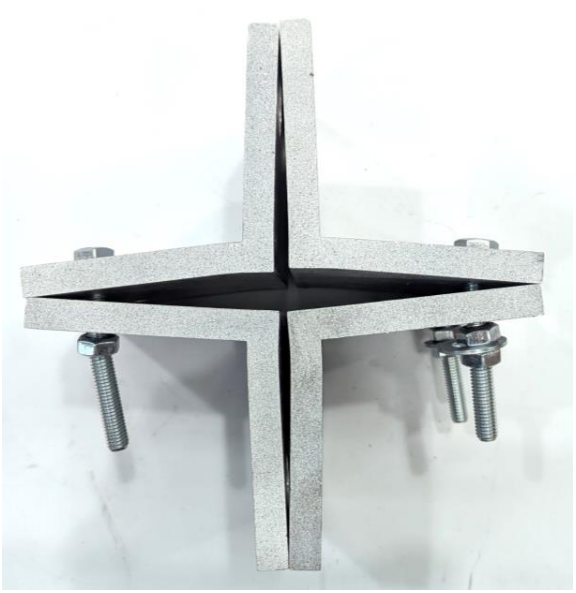

Bolt fracture (B)
(c)

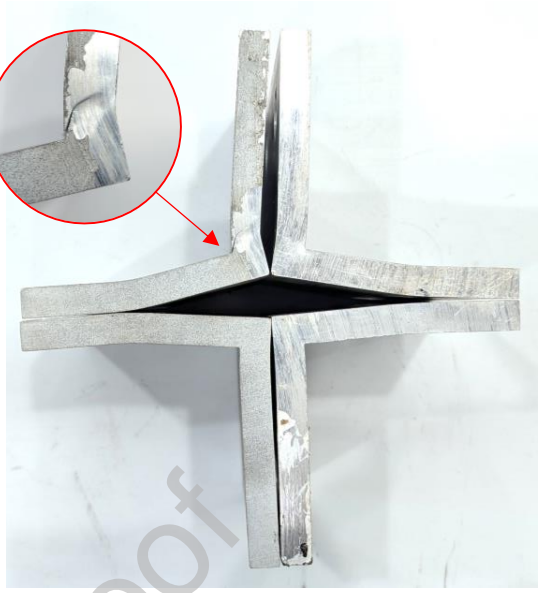

Web fracture (W)
(d)

Figure 10: Failure modes for specimen (a) M10-6.2-21.6-R-1&2; (b) M10-6.2-41.6-S; (c) M10-12.7-21.6-S; (d) M16-12.7-41.6-S.

3. NUMERICAL MODELLING

3.1 Description of the model

A numerical model using the general-purpose Finite Element (FE) software ABAQUS [30] was developed following the modelling assumptions reported in similar studies [8,10,11]. Eight-noded linear solid elements with reduced integration C3D8R were adopted to discretise the geometry of the angle cleats and bolts. Mesh refinement was applied into the fracture zone, as shown in Figure 11, to allow the stress triaxiality and the plastic strain and hence the fracture process to be accurately captured. Similarly, the mesh discretising the bolts was also fine since bolt fracture was also a possibility explicitly considered in the modelling. The rigid plate for specimens in the (R) configuration was more coarsely meshed as it did not affect significantly the structural response and the stress predictions within the plate were of lesser importance. For all the analyses conducted, at least 3 solid elements through the flange thickness were adopted to capture the flexural deformations and avoid shear locking, in line with previous recommendations [8, 10, 11]. To reduce computational time, the symmetry of the specimens in terms of geometry, loading and boundary conditions was exploited and therefore only ¼ of the models was considered. Initial

imperfections were not considered in the models since there was no deviation from the right angle in the supplied angle cleats and customarily are not considered in connection modelling.

A discretized quarter model of a specimen tested in the (R) arrangement is shown in Figure 11 (a) and (b), where the symmetry planes and boundary conditions are also depicted. The applied boundary conditions restrained the movement perpendicular to the symmetry planes, whilst the vertical displacement was restrained at the lower face of the rigid plate. The load was applied through the loading plate as a prescribed vertical displacement higher than the one achieved during testing. For specimens in the (S) configuration shown in Figure 11 (c), the modelling approach was similar, except that in place of the rigid plate the symmetric lower angle cleat and its loading plate was explicitly modelled, and the vertical displacement of the model was restrained across the bottom face of the lower loading plate, as shown in Figure 11 (d). "All* with self" contact interaction was applied to the models, using a friction coefficient of 0.25 and "penalty" formulation in the tangential behaviour and "hard" contact in the normal behaviour. Separation after contact was allowed. Kinematic coupling was assigned to the top face of the loading plate, constraining all degrees of freedom and defining RP1 as the controlling point.

The bolt geometry was simplified to reduce computation time and the modelling complexity. The bolt thread was modelled as a cylinder with an effective diameter equivalent to the stress area of the threaded bolts. The bolt head and nut were modelled as a single piece along with the bolt shank, and the hexagonal shape of the bolt head and nut were simplified as cylinders. These simplifications have been adopted in the literature without affecting the accuracy of the results [10, 11, 31]. No bolt preload was applied, given that in the tests the bolts were hand-tightened to obtain the snug-tight condition.

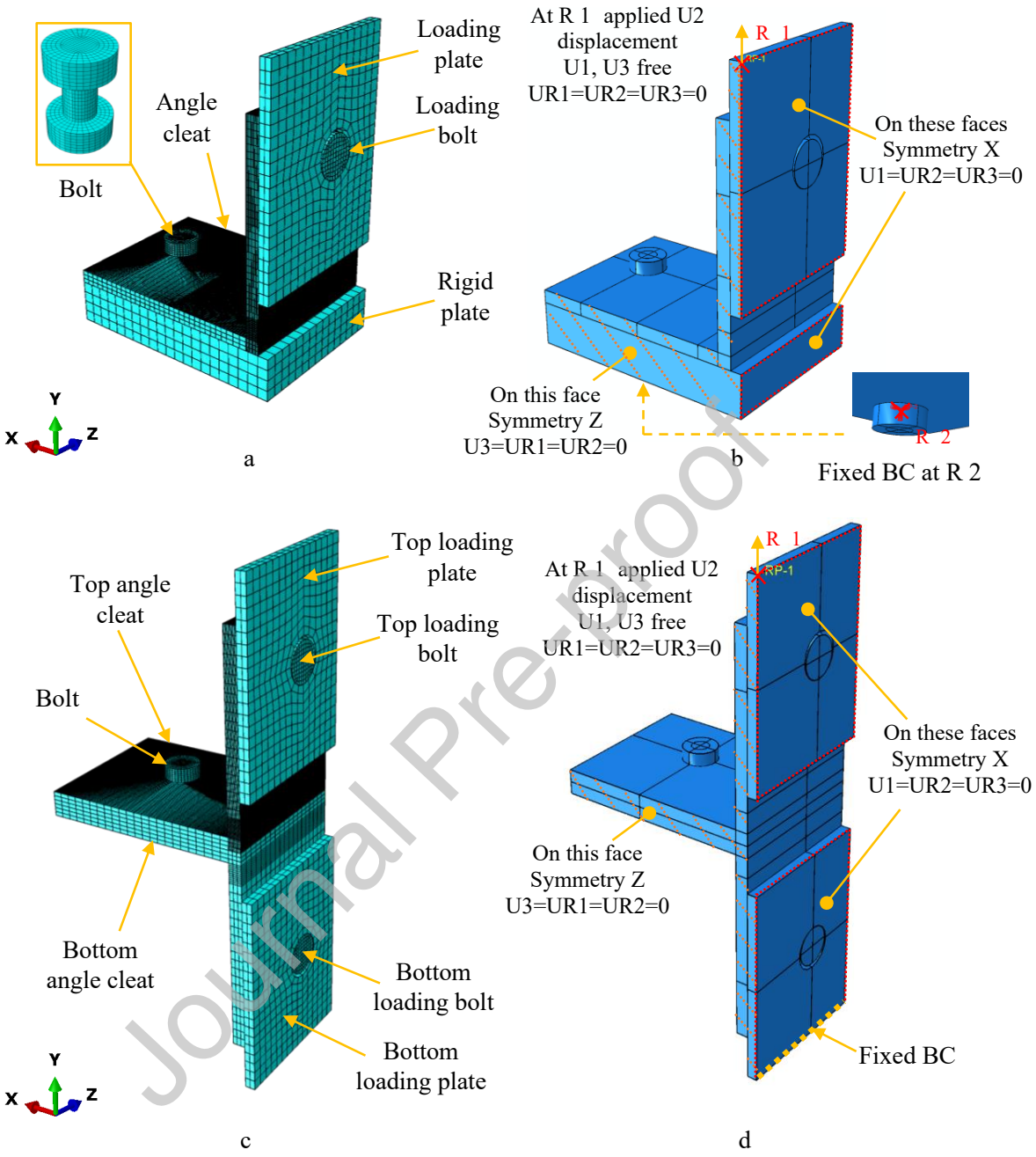

Figure 11: FE (a) model parts; (b) boundary conditions for specimens in (R) configuration; (c) model parts; (d) boundary conditions for specimens in (S) configuration.

For all models a quasi-static explicit dynamic analysis was conducted to allow fracture to be captured without convergence issues within a manageable timeframe. To this end, mass scaling

was employed to increase the stable time increment and hence reduce the overall computation time, whilst a smooth amplitude curve [30] was employed to apply the prescribed vertical displacement whilst minimising the inertia effects on the model. The suitability of the employed scheme was verified by ensuring that the kinetic energy remained a small fraction (less than 2%) of the internal energy throughout most of the analysis time.

3.2 Material modelling and fracture

The bolt material properties and fracture model adopted herein for Grade 8.8 bolts were taken from [27], where fracture studies on bolts from the same batch as the ones used herein were reported. No fracture model was defined for the Grade 10.9 bolt since it remained elastic throughout the test. The obtained material coupon stress-strain curves reported in Table 2 for 6082 T6 were converted into true stress and logarithmic plastic strain and incorporated into the FE model to define the material response up to the attainment of the ultimate tensile stress (i.e. within the uniform plasticity material region).

Replicating the post-necking response of coupons is challenging given the localization and complexity of strains and stresses in the necked region. The post-necking material response was modelled based on an iterative modelling approach termed the mixed weighted average method, originally proposed in [32]. The main underlying assumption is that the post-necking material response can be approximated as the weighted average of a power law extrapolation and a linear extrapolation of the material response beyond necking, which are considered to be lower and upper bounds respectively of the actual post-necking stress-strain response. This is defined in Eq. (12):

$$\sigma = \sigma_u \left[w(1 + \varepsilon - \varepsilon_u) + (1 - w) \left(\frac{\varepsilon^{\varepsilon_u}}{\varepsilon_u^{\varepsilon_u}} \right) \right] \quad (12)$$

where σ and ε are the true stress and true strain values of the post-necking material response, σ_u and ε_u are the true stress and true strain at necking, and w and (1-w) are the weighting factors determined through an iterative trial and error approach until the numerical material response is in close agreement with the experimental load-displacement curves reported in Figure 7.

Figure 12 shows the experimental and numerical curves for the dog bone and flat grooved specimens obtained for a weighting factor w=0.3 which leads to the best agreement with the experimental results and is used subsequently for all numerical analyses. Upon successfully replicating the load-displacement curve of the material coupons, a fracture model is calibrated using the experimental curves reported in Figure 7 and assuming that the strain at fracture is a function of the stress triaxiality. The triaxiality value at the centre of the specimen, where fracture initiates versus the equivalent plastic strain (PEEQ), is presented in Figure 13 (a) for the tested flat grooved specimens, where it can be seen that the peak stress triaxiality increases with the radius of the notch. The average triaxiality for each flat-grooved specimen was calculated as the area under the curve showing the evolution of triaxiality at the centre of the specimens with plastic strain, normalized by the PEEQ at fracture ε_f as given in Eq. (13), where η_{av} is average stress triaxiality, ε is the equivalent strain and ε_f is the equivalent strain to fracture.

$$\eta_{av} = \frac{1}{\varepsilon_f}\int_0^{\varepsilon_f} \eta(\varepsilon)d\varepsilon \qquad 13$$

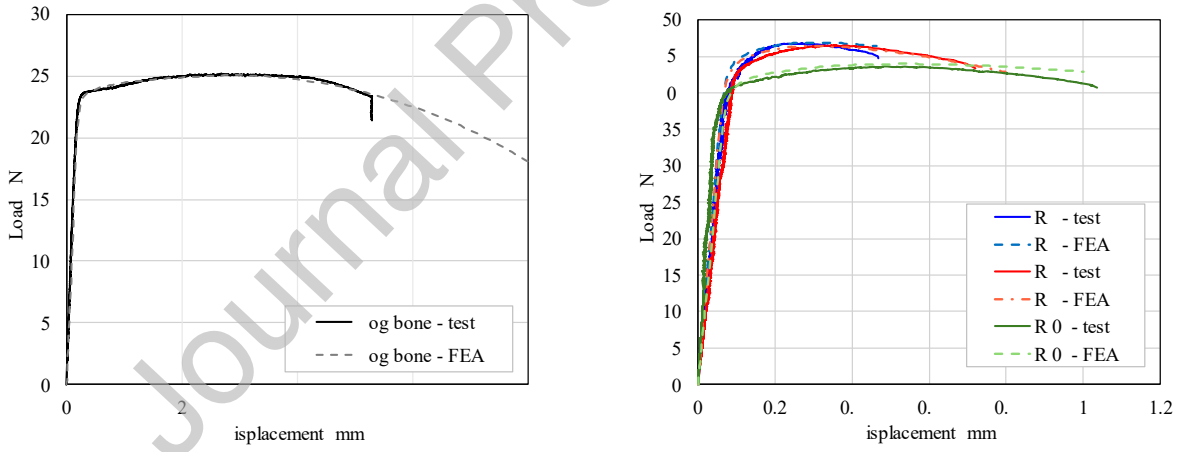

(a) (b)

Figure 12: Experimental and numerical curves for (a) dog bone; (b) flat grooved specimens obtained for a weighting factor w=0.3.

The relationship between the stress triaxiality η and the equivalent plastic strain at fracture ε_f is shown in Figure 13 (b) as well as the best fit curve defined by Eq. (14). This curve is used as a

fracture initiation criterion using the ductile damage material option in ABAQUS and specifying a very low (virtually zero) energy for the fracture propagation.

$$\varepsilon_f = 10.682e^{-5.064\eta} \qquad 1$$

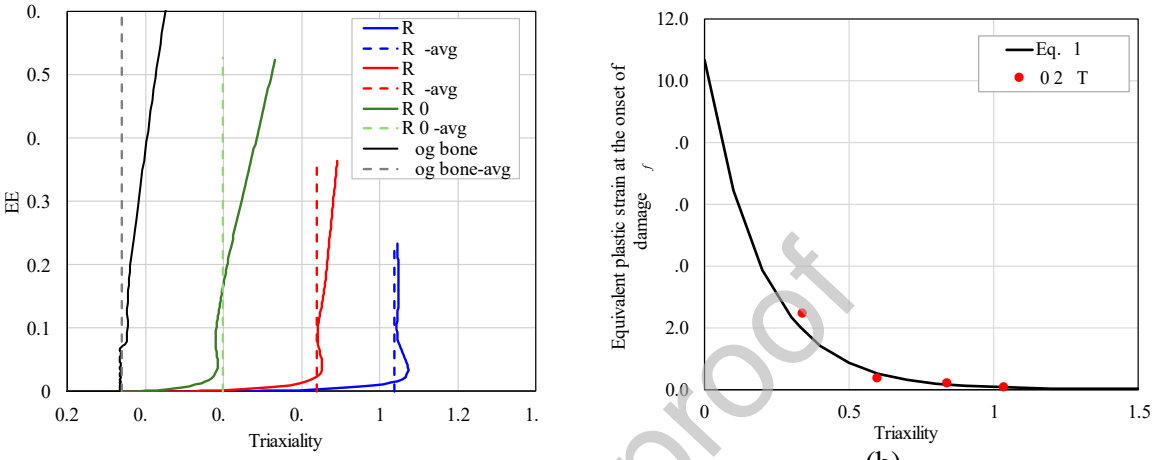

Figure 13: (a) Evolution of stress triaxiality with plastic strain until fracture initiation; (b) equivalent plastic strain at fracture as a function of stress triaxiality bolts and proposed equation.

3.3 Validation

The developed FE model incorporating fracture is validated herein by comparing the numerically obtained load-displacement curves and failure modes with the previously reported experimental ones, as shown in Figure 14. Overall, the numerically predicted load-displacement curves are in close agreement with the experimental ones and the fracture is well captured by the FE models. The mean value of the numerical over experimental ultimate load for all five tests is 1.04 with a coefficient of variation of 0.03. The agreement of the experimental and numerical curves is close for all specimens indicating the suitability of the employed fracture model to predict fracture for both the 6082 T6 cleat material and the Grade 8.8 bolts.

Moreover, the comparison between the full-field strain measurements obtained from the DIC system and the numerical strain fields for the maximum principal strain are in good agreement. From both experimental and numerical results, it is clearly observed that there is significant strain

localisation on the inner side of the vertical cleat leg. This is caused by the combined effects of tensile forces from the applied tension and tensile forces due to bending. In Figure 14 (a), the experimental curves show a more gradual loss of strength before fracture compared to the numerical results. This difference arises because, in the experiments, factors such as asymmetries, loading eccentricities, and material variability caused fracture to initiate on one side of a single angle cleat and propagated progressively. In contrast, the FE models did not account for such variability, leading to simultaneous fracture along the entire length of both angle cleats and a correspondingly more abrupt loss of strength.

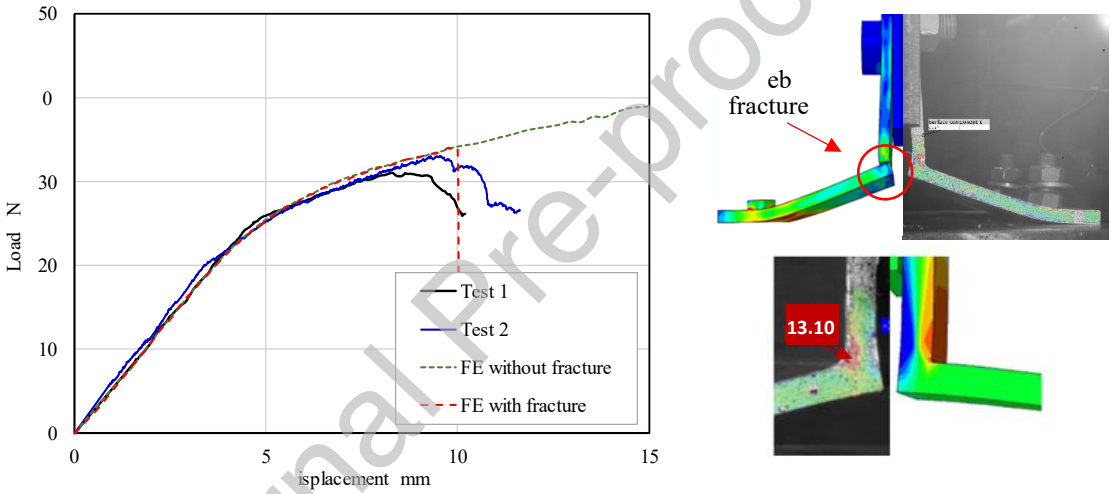

(a) M10-6.2-21.6-R-1 & 2

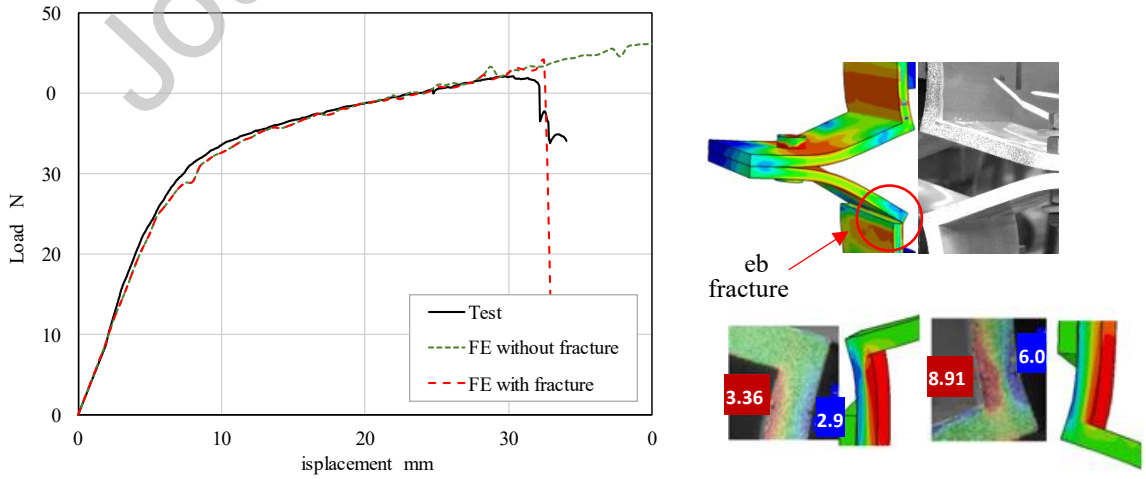

(b) M10-6.2-41.6-S

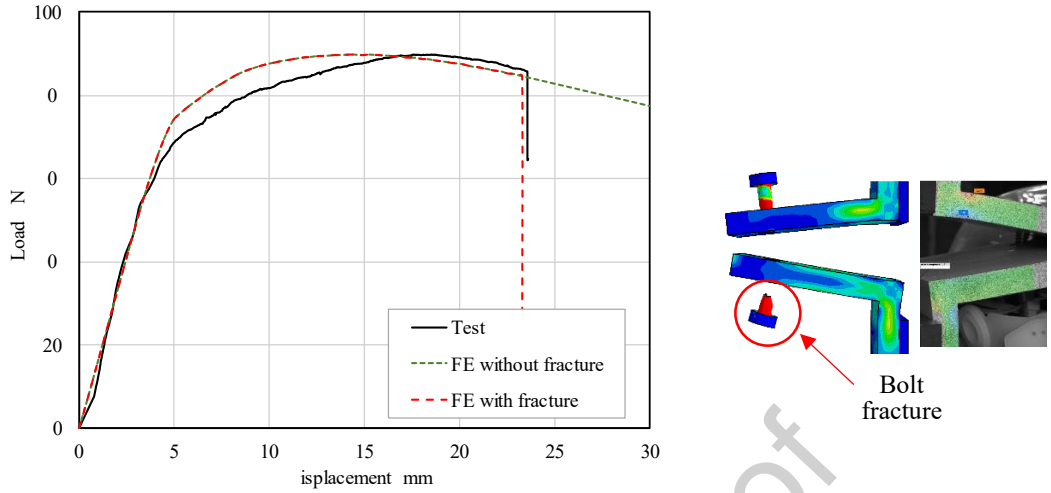

(c) M10-12.7-21.6-S

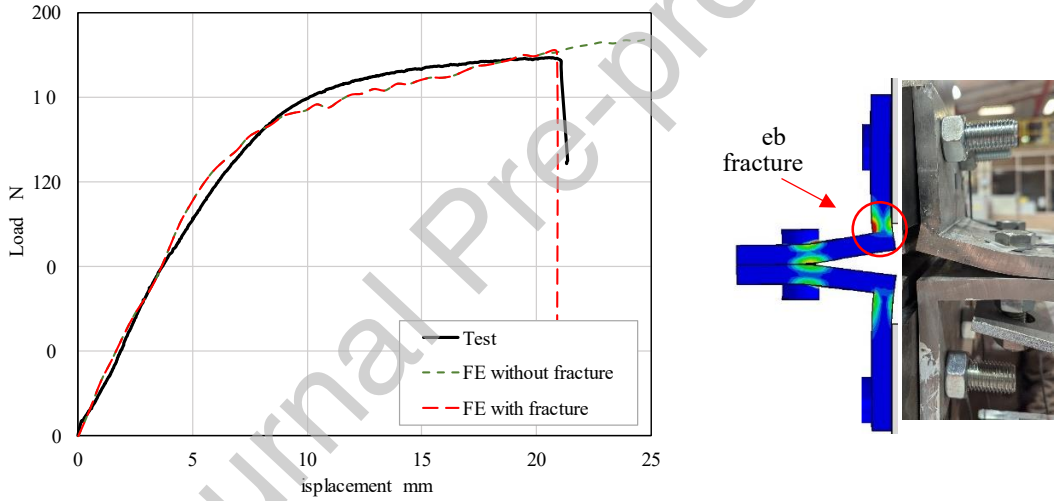

(d) M16-12.7-41.6-S

Figure 1 : Comparison of the numerical force-displacement curves and failure mode with the experimental curves using the material plasticity-based method

3.4 Parametric studies and discussion

Having validated the numerical model, 20 FE parametric models using the rigid plate arrangement were created based on the calibrated material and fracture parameters to explore the effects of angle thickness, bolt diameter, and bolt distance to edge on the ultimate response of the bolted angle cleat. All models employ the material model (including fracture) for 6082 T6 previously discussed and the bolt material model for Grade 8.8 bolts developed in [27]. The results are then

used to assess the suitability of the equivalent T-stub model for predicting the ultimate response of aluminium bolted flange cleats in bending. The numerical resistances are reported in Table 5 together with the design predictions of EN 1999-1-1 [3] with all partial safety factors set to unity, and the proposed method discussed hereafter. In bold are the design predictions that are unsafe.

Table 5. Assessment of EN 1999-1-1 [3] based on the parametric study and proposed method.

No.	Bolt diameter	t (mm)	e_e (mm)	$F_{u,FE}$ (kN)	$F_{u,EC9}$ (kN)	Failure mode EC9	$F_{u,EC9}/F_{u,FE}$	$F_{u,mod}$ (kN)	$F_{u,mod}/F_{u,FE}$	Failure mode proposed
1	M10	6	25	19.2	15.7	1	0.82	15.2	0.79	1
2	M10	12	25	69.8	67.2	1	0.96	62.9	0.90	1
3	M10	18	25	107.6	108.5	2b	**1.01**	96.6	0.90	2b
4	M10	24	25	142.5	163.8	2b	**1.15**	137.8	0.97	2b
5	M10	30	25	190.1	203.4	3	**1.07**	191.1	1.00	2b
6	M10	6	50	31.7	21.8	1	0.69	20.9	0.66	1
7	M10	12	50	96.2	96.2	1	1.00	87.6	0.91	1
8	M10	18	50	156.8	158.4	2b	**1.01**	143.2	0.91	2b
9	M10	24	50	195.5	203.4	2b	**1.04**	186.2	0.95	2b
10	M10	30	50	223.0	203.4	3	0.91	203.4	0.91	3
11	M16	6	25	21.5	15.7	1	0.73	15.2	0.71	1
12	M16	12	25	69.9	67.2	1	0.96	62.9	0.90	1
13	M16	18	25	144.8	163.1	1	**1.13**	146.9	**1.01**	1
14	M16	24	25	215.7	254.2	2b	**1.18**	220.4	**1.02**	2b
15	M16	30	25	256.6	337.7	2b	**1.32**	277.2	**1.08**	2b
16	M16	6	50	34.7	21.8	1	0.63	20.9	0.60	1
17	M16	12	50	100.1	96.2	1	0.96	87.6	0.88	1
18	M16	18	50	207.6	241.4	1	**1.16**	208.2	1.00	1
19	M16	24	50	331.8	397.1	2a	**1.20**	350.9	**1.06**	2a
20	M16	30	50	429.5	490.6	2a	**1.14**	414.4	0.96	2b
					All	Mean	1.00		0.91	
						COV	0.18		0.14	
					mode 1	Mean	0.90		0.84	

No.	Bolt diameter	t (mm)	e_e (mm)	$F_{u,FE}$ (kN)	$F_{u,EC9}$ (kN)	Failure mode EC9	$F_{u,EC9}/F_{u,FE}$	$F_{u,mod}$ (kN)	$F_{u,mod}/F_{u,FE}$	Failure mode proposed
						COV	0.20		0.17	
					mode 2	Mean	1.14		0.98	
						COV	0.09		0.06	

Overall, the ratio of the ultimate load predicted by the equivalent T-stub model [3] over the numerical one $F_{u,EC9}/F_{u,FE}$ is 1.00 with a COV of 0.18, indicating a high scatter in the design predictions. The mean value and COV of the $F_{u,EC9}/F_{u,FE}$ ratio for flange cleats predicted to fail in mode 1 (i.e. plastic failure of the flange) is 0.90 and 0.20 respectively, whilst these values become 1.13 and 0.09 for modes 2a (i.e. plastic failure of the flange at the web to flange junction and yielding of the bolts) and 2b (i.e. bolt failure and yielding of the flange). It can be seen that the design predictions for flange cleats using the equivalent T-stub model become increasingly unsafe with increasing flange thickness. This is believed to relate to the fact that with increasing flange thickness, the bending resistance of the flange cleats increases more rapidly than its resistance to tension, thus the effect of the coexisting axial tension is more detrimental for thick angle cleats. The co-existing tensile force in addition to the bending moment in the vertical cleat leg at the junction with the horizontal one leads to higher tensile stresses and premature fracture and is not considered by the T-stub model, thereby resulting in unsafe predictions for thick angle cleats.

4. DESIGN RECOMMENDATIONS FOR ALUMINIUM ANGLE CLEATS

To rectify the observed dependency of the reliability of the predictions of the T-stub model on the cleat thickness, a simple remedy is proposed herein, which considers the effect of the tensile force acting on the vertical angle cleat. The approach specified in EN 1999-1-1 [3] is also employed herein, however the determination of the plastic moment resistance and ultimate moment resistance $M_{w,o}$ and $M_{w,u}$ of the cleat web is modified according to Equations (15) and (16):

$$M_{w,u} = \frac{2b(t_w - t_{eff,u})^2}{4} f_u \frac{1}{k} \quad (15)$$

$$M_{w,o} = \frac{2b(t_w - t_{eff,o})^2}{4} f_u \frac{1}{k} \quad (1)$$

Where l_{eff} is the length of the angle cleat, t_w is the cleat web thickness,1/k is a material related parameter given in [3]. The moment resistance of the flange of the angle cleat remains unchanged. The newly introduced symbols $t_{eff,0}$ and $t_{eff,u}$ are the effective web thicknesses contributing to the plastic moment resistance $M_{w,0}$ and the ultimate moment resistance $M_{w,u}$ of the web of the angle cleat respectively. The assumed stress distribution within the web of the angle cleat at failure is shown in Figure 15 by the dotted line. The part of the thickness designated as t_{eff} is contributing to the moment resistance of the web and the remaining thickness (t_w - t_{eff}) is resisting the tensile force. The numerically obtained stress contour plot of the web section of a 24mm thick angle cleat (model 9) in Figure 16. The stress contours plotted in Figure 16 (a) correspond to a cross-section of the web just above the flange to web junction; only one half of the cleat width is shown for clarity, exploiting symmetry. The stress distribution at mid-width of the angle cleat is also depicted in Figure 16 (b), where a clear asymmetry between the compressive and the tensile stresses can be observed, which roughly agrees with the assumptions depicted in Figure 15. The increment at which the numerical results were extracted was the one just prior to fracture which corresponds to the ultimate load. It is noted that the stress distribution depicted in Figure 16 (b) has a significant linear (elastic) region within approximately half of the web thickness. This is due to the results being extracted at a small number (100) of equally spaced time intervals out of the thousands of time increments of the analysis for computational efficiency; hence results just prior to fracture which would have a more uniform stress distribution were not obtained closer to the one shown in Figure 15.

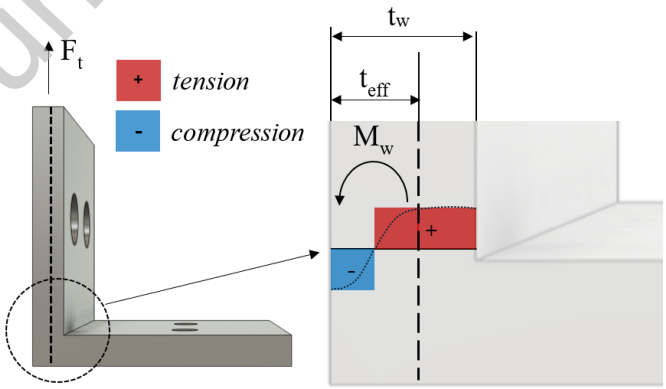

Figure 15: Assumed stress distribution within the web of the angle cleat at failure.

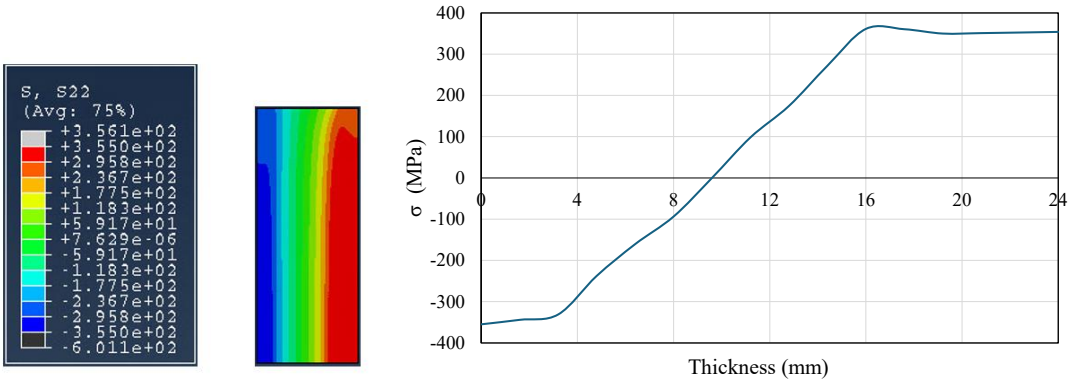

(a) Stress contour plot at web (b) through web thickness stress distribution

Figure 16: FE obtained normal stress distribution through web thickness for model 9

The effective thickness t_{eff} can be determined by equating the tensile resistance of the area of the angle cleat resisting the tensile force $[b(t_w - t_{eff})]$ to the failure load F_u for each failure mode. For mode 1 the failure load is given by Eq. (17):

$$F_{u,1} = 2b\left(t_w - t_{eff,u,1}\right)f_u\frac{1}{k} = \frac{2(M_{u,1})_w + 2(M_{u,1})_b}{g} \tag{17}$$

Substituting Eq. (17) for $(M_{u,1})_w$ in Eq. (15) results in a second degree polynomial equation and the unknown effective thickness $t_{eff,u}$ can be explicitly determined from Eq. (18):

$$t_{eff,u,1} = -2g + \sqrt{4g^2 + 4gt_w - {t_w}^2} \tag{18}$$

Similarly, the effective thicknesses $t_{eff,u,2}$ and $t_{eff,0,2}$ corresponding to modes 2a and 2b are given by Equations (19) and (20) respectively:

$$t_{eff,u,2} = -(g + e_e) + \sqrt{(g + e_e)^2 + 2(g + e_e)t_w - \frac{e_e\sum B_0}{bf_u\frac{1}{k}}} \tag{19}$$

$$t_{eff,0,2} = -(g + e_e) + \sqrt{(g + e_e)^2 + 2(g + e_e)t_w - \frac{e_e\sum B_u}{bf_0}} \tag{20}$$

Following the determination of the effective thicknesses corresponding to modes 1, 2a and 2b, the corresponding resistances $F_{u,1}$, $F_{u,2a}$ and $F_{u,2b}$ are calculated with the resistance corresponding to mode 3 remaining unchanged. The minimum of the four resistances is the design prediction $F_{u,mod}$ according to the modification to the EN 1999-1-1 [3] proposed herein. The resulting design prediction $F_{u,mod}$, the ratio of the predicted over numerically obtained resistance $F_{u,mod}/F_{u,FE}$ and the corresponding predicted failure modes are reported in Table 5. On average, the proposed method is underpredicting the resistance of the bolted cleats by 9% with a coefficient of variation of 0.14. More importantly, contrary to the EN 1999-1-1 [3] design method, the proposed method results in generally safe predictions, with a maximum overprediction of 8%.

Comparing the two methods for the different failure modes, it can be clearly seen that the proposed method is slightly more conservative and more consistent for cleats failing in mode 1, but significantly more conservative and consistent for thicker specimens failing in mode 2. This is clearly visualised in Figure 17, where the predicted over numerical strength ratio is plotted on vertical axis with the thickness of the angle cleat shown on the horizontal axis.

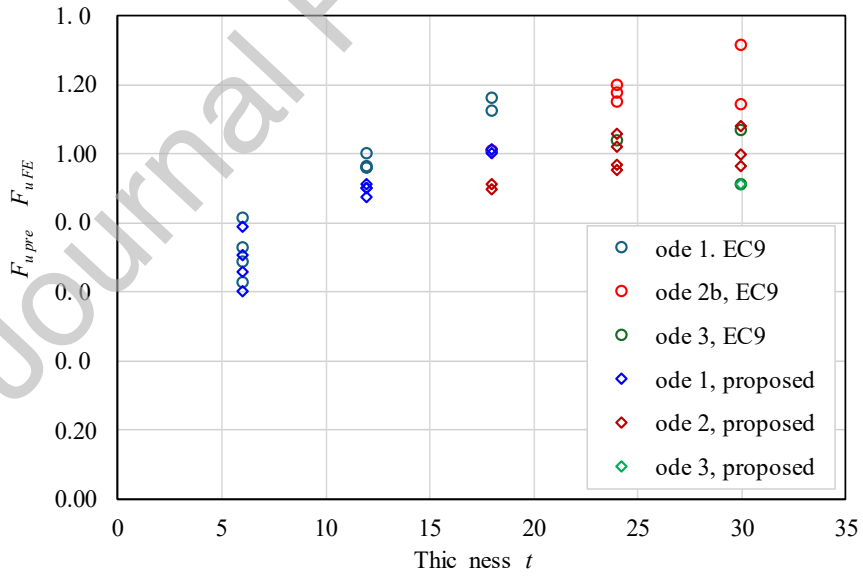

Figure 17: Assessment of design methods for various failure modes.

5. CONCLUSIONS

The experimental and numerical research reported herein showed that using the equivalent T-stub method for the prediction of the resistance of aluminium bolted cleats becomes unsafe with increasing cleat thickness, due to the effect of the coexisting axial tension acting on one leg of the angle cleat. Since the EN 1999-1-1 resistance model employs the ultimate stress, there is no reserve strength to accommodate the extra tensile stresses, thus leading to increasingly unsafe ultimate capacity predictions. A simple modification to the current method is proposed herein which considers that, unlike in the traditional T-stub model, failure happens in the angle cleat web. The proposed approach adopts the same overall assumptions but explicitly accounts for the effect of the tensile force on the resistance of the angle cleat web. It does so by assuming that a portion of the web thickness resists the tensile force, while the remaining thickness is effective in resisting the moment. It utilises explicit equations derived from first principles and is shown to offer improved ultimate capacity predictions both in terms of safety as well as in terms of consistency. It is therefore recommended that the proposed method be adopted in future revisions of EN 1999-1-1 for the determination of the ultimate resistance of bolted angle cleats.

ACKNOWLEDGEMENTS

The research presented in this article has received funding from the Smart Concept Fund of the European Regional Development Fund (ERDF) from the European Union (EU). The authors are grateful for the support in the laboratory provided by Miss Kathryn Nicoll.

REFERENCES

[1] Siwowski, T., Aluminium Bridges - Past, Present and Future. Structural Engineering International, 16:4, 286-293, 2006.

[2] Georgantzia, E., Gkantou, M., and Kamaris, G., Aluminium alloys as structural material: A review of research. Engineering Structures, 227, 111372, 2021.

[3] European Committee for Standardization, Eurocode 9: Design of aluminium structures, in Part 1-1: General structural rules. CEN: Brussels, 2023.

[4] European Committee for Standardization, Eurocode 3: Design of aluminium structures, in Part 1-8: Design of Joints. CEN: Brussels, 2023.

[5] Girao Coelho, A.-M., Bijlaard, F.S.K., Gresnigt, N. and da Silva, L.S., Experimental assessment of the behaviour of bolted T-stub connections made up of welded plates. Journal of Constructional Steel Research, 60, 269-311, 2004.

[6] Zhao M.S., Lee C.K., and Chiew S., Tensile behavior of high performance structural steel T-stub joints. Journal of Constructional Steel Research, 122, 316-325, 2016.

[7] Yuan H.X., Hu S., Du X.X., Yang L., Cheng X.Y., Theofanous M., Experimental behaviour of stainless steel bolted T-stub connections under monotonic loading, Journal of Constructional Steel Research, 152, 213–224, 2019.

[8] Yuan, H.X., Gao, J.D., Theofanous, M., Yang, L., Schafer, B.W., Initial stiffness and plastic resistance of bolted stainless steel T-stubs in tension, Journal of Constructional Steel Research, 173, 106239, 2020.

[9] Yapici, O., Theofanous, M., Yuan, H.X., Skalomenos, K. and Dirar, S., Experimental study of ferritic stainless steel bolted T-stubs under monotonic loading, Journal of Constructional Steel Research, 183, 106761, 2021.

[10] Yapici, O., Theofanous, M., Afshan, S., Yuan, H.X., and Dirar, S., Numerical modelling of stainless steel bolted T-stubs in tension, Thin-Walled Structures, 177, 109432, 2022.

[11] Yapici, O., Theofanous, M., Yuan, H.X., Dirar, S. and Afshan, S., Numerical simulation and design of ferritic stainless steel bolted T-stubs in tension. Journal of Constructional Steel Research ,198, 107555, 2022.

[12] Yuan H.X., Liu X.H., Liu J.L., Theofanous M. Cyclic behaviour and hysteretic model of austenitic stainless steel bolted T-stubs. Journal of Constructional Steel Research, 182, 106659, 2021.

[13] Elflah, M.,Theofanous, M., Dirar, S. and Yuan H.X., Behaviour of stainless steel beam-to-column joints — Part 1: Experimental investigation. Journal of Constructional Steel Research, 152, 183-193, 2019.

[14] Gao, J.D., Yuan, H.X., Du, X.X., Hu, X.B. and Theofanous, M., Structural behaviour of stainless steel double extended end-plate beam-to-column joints under monotonic loading, Thin-Walled Structures, 151, 106743, 2020.

[15] Gao, J.D., Du, X.X., Yuan, H.X, and Theofanous, M., Hysteretic performance of stainless steel double extended end-plate beam-to-column joints subject to cyclic loading. Thin-Walled Structures, 164, 107787, 2021.

[16] De Matteis, G., Della Corte, G. and Mazzolani, F., Experimental analysis of aluminium T-stubs: tests under monotonic loading, XVIII Congresso CTA. ACS ACAI Servizi srl. 29-40, 2001.

[17] De Matteis, G., Della Corte, G. and Mazzolani, F., Experimental analysis of aluminium T-stubs: tests under cyclic loading, The International Conference on Advances in Structures. Sydney, Australia, 2003.

[18] De Matteis, G., Brescia, M., Formisano, A. and Mazzolani, F., Behaviour of welded aluminium T-stub joints under monotonic loading. Computers & Structures, 87, 990-1002, 2009.

[19] De Matteis, G., Naqash, N. and Brando, N., Effective Length of Aluminium T-Stub Connections by Parametric Analysis. Engineering Structures, 41, 548-461, 2012.

[20] Xu, H., X. Guo, and Y. Luo, The Load-Bearing Capacity of Aluminum Alloy T-Stub Joints. Advanced Materials Research, 261,765-769, 2011.

[21] Wang Z., Wang Y., Zhang Y., Gardner L., Ouyang Y. Experimental investigation and design of extruded aluminium alloy T-stubs connected by swage-locking pins. Engineering Structures, 200, 109675, 2019.

[22] Yang, S., Wang, Y., Yang, X., Lu, X., Li, M. V., & Zhu, X. Effect of softening of 6082-T6 aluminum alloy CMT welded joints on mechanical properties and fracture behavior. Journal of Manufacturing Processes, 124, 1567-1582, 2024.

[23] Yang, S., Yang, X., Lu, X., Li, M. V., Zuo, H., & Wang, Y. Strength calculation and microstructure characterization of HAZ softening area in 6082-T6 aluminum alloy CMT welded joints. Materials Today Communications, 37, 107077, 2023.

[24] Elghazouli AY, Málaga-Chuquitaype C, Castro JM and Orton AH. Experimental monotonic and cyclic behaviour of blind-bolted angle connections. Engineering Structures, 31(11), 2540-2553, 2009.

[25] Málaga-Chuquitaype C. and Elghazouli AY. Behaviour of combined channel/angle connections to tubular columns under monotonic and cyclic loading. Engineering Structures, 32(6), 1600-1616, 2010.

[26] Bock M, Theofanous M, Dirar S and Lipitkas N. Aluminium SHS and RHS subjected to biaxial bending: Experimental testing, modelling and design recommendations. Engineering Structures 2021, 227 (15), 111468

[27] Yapici O., Theofanous, M.,Yuan, H.X, Afshan, S., Skalomenos K., Comparative study on fracture characteristics of carbon and stainless steel bolt material. Journal of Constructional Steel Research, 210, 108102, 2023.

[28] Bai Y., Teng X. and Wierzbicki T. On the Application of Stress Triaxiality Formula for Plane Strain Fracture Testing. Journal of Engineering Materials and Technology-transactions of The ASME, 131(2), 021002, 2009.

[29] Zhou, J., Yan, S., Rasmussen, K.J.R., Zhang, M. Test-and-FE-based method for obtaining complete stress-strain curves of structural steels including fracture. Journal of Constructional Steel Research, 2025, 224(A), 109095.

[30] Systemes, ., BA US Standard user's manual volumes I-III and ABAQUS CAE manual - Version 6.19. 2014: Simulia Corporation.

[31] Cabrera, M., Tizani, W., & Ninic, J. Fusion of experimental and numerical data for development of Extended Hollo-bolt component based model. Engineering Structures, 321, 118932, 2024.

[32] Ling Y. Uniaxial true stress-strain after necking. AMP Journal of Technology, 5, 37-48, 1996.

Author statement

Dr Manuela Cabrera: Methodology, Software, Validation, Formal Analysis, Investigation, Visualization, Data Curation, Data Curation, Writing – Original Draft, Writing – Review & Editing.

Dr Marios Theofanous: Conceptualization, Methodology, Software, Validation, Formal Analysis, Investigation, Resources, Data Curation, Writing – Original Draft, Writing – Review & Editing.

Dr Marina Bock: Funding acquisition, project administration, Supervision, Visualization, Resources, Data Curation, Writing – Original Draft, Writing – Review & Editing.

Declaration of interests

☐ The authors declare that they have no known competing financial interests or personal relationships that could have appeared to influence the work reported in this paper.

☒ The authors declare the following financial interests/personal relationships which may be considered as potential competing interests:

Marina Bock reports financial support was provided by European Regional Development Fund. If there are other authors, they declare that they have no known competing financial interests or personal relationships that could have appeared to influence the work reported in this paper.